Journal of Nuclear Materials xxx (2009) xxx–xxx

Contents lists available at ScienceDirect

Journal of Nuclear Materials

journal homepage: www.elsevier.com/locate/jnucmat

Identification and quantification of hydride phases in Zircaloy-4 cladding using synchrotron X-ray diffraction ☆

R.S. Daum [a,1], Y.S. Chu [b,2], A.T. Motta [c,*]

[a] Nuclear Engineering Division, Argonne National Laboratory, Argonne, IL 60439, United States
[b] X-ray Science Division, Argonne National Laboratory, Argonne, IL 60439, United States
[c] Department of Mechanical and Nuclear Engineering, The Pennsylvania State University, University Park, PA 16802, United States

ARTICLE INFO

Article history:
Received 20 November 2008
Accepted 7 April 2009
Available online xxxx

ABSTRACT

Zirconium hydrides precipitate in fuel cladding alloys as a result of hydrogen uptake from the high-temperature corrosion environment of light water reactors. Synchrotron X-ray diffraction was performed at room temperature on stress-relieved Zircaloy-4 cladding with two distributions of hydrides – (1) uniformly distributed hydrides across the entire cladding wall and (2) hydride rim next to the outer surface. The δ-hydride phase was found to be the predominant hydride phase to precipitate for hydrogen contents up to 1250 weight parts per million (wt ppm). At a higher content, about 3000 wt ppm, although δ-hydride is still the majority phase, a significant amount of γ-hydride is also observed. At even higher hydrogen contents, in excess of approximately 6000 wt ppm, such as can occur in a highly dense hydride layer, peaks associated with the ε-hydride phase are also observed in the diffraction pattern. The volume fraction of hydrides was estimated as a function of hydrogen content using the integrated intensities of select diffraction peaks corresponding to the α-Zr matrix and the hydride phases. These estimated values agree well with calculated values from the independently measured concentrations. The results of this study indicate that hydride precipitation in Zircaloy-4 is a complex process of evolving hydride phases with increasing local hydrogen content.

1. Introduction

During operation of a light water reactor (LWR), the mechanical behavior of the zirconium-based fuel cladding degrades due to a combination of oxidation, hydriding, and radiation damage [1]. In an effort to increase operating efficiency through the use of longer fuel cycles, and to reduce the volume of waste, utilities have a strong economic incentive to increase the average discharge burnup of the fuel assemblies to >45 GWd/MTU (i.e., threshold for high burnup) [2]. However, longer exposure to the reactor environment exacerbates cladding degradation, which may increase the likelihood of cladding failure during postulated design-basis accidents [3].

Waterside corrosion of the Zr alloy cladding results in hydrogen uptake and subsequent formation of second phase hydrides. The presence of these hydrides has been shown to reduce cladding ductility. For Zircaloy-4, 10–20% of the hydrogen liberated from corrosion is typically absorbed into the cladding [4,5]. The terminal solid solubility of hydrogen in Zircaloy-4 is less than 10 weight parts per million (wt ppm) at room temperature and between 50 and 100 wt ppm at normal operating temperatures of a PWR (≈320 °C) [6,7]. When the solubility is exceeded, elongated hydride platelets precipitate with major axes along the transverse (i.e., circumferential) and longitudinal (i.e., axial) directions of the cladding. In the absence of loading during hydride precipitation this orientation is believed to be primarily determined by the direction of compressive strains in the last deformation pass [8]. Because the cladding texture is also dependent on the compressive stress direction, there is a coincidence between the Zr and hydride orientations.

In zirconium, the hydride platelets are found to be predominantly δ-hydride (face-centered cubic; ZrH_x, where $1.59 \leqslant x \leqslant 1.66$, $c_o/a_o = 1$) but, upon cooling quickly (i.e., water and oil quench), a metastable γ-hydride (face-centered tetragonal; ZrH with $c_o/a_o > 1$) may also form [9,10]; it is worth noting that the volume increase (i.e., dilation strain) due to the precipitation of δ-hydride and γ-hydride in α-Zr is 17.2% and 12.3%, respectively [11]. One study showed that, regardless of cooling rate, the

☆ The submitted manuscript has been created by UChicago Argonne, LLC, Operator of Argonne National Laboratory ('Argonne'). Argonne, a US Department of Energy Office of Science laboratory, is operated under Contract No. DE-AC02-06CH11357. The US Government retains for itself, and others acting on its behalf, a paid-up nonexclusive, irrevocable worldwide license in said article to reproduce, prepare derivative works, distribute copies to the public, and perform publicly and display publicly, by or on behalf of the Government.

* Corresponding author. Address: Department of Mechanical and Nuclear Engineering, The Pennsylvania State University, 227 Reber Building, University Park, PA 16802, United States. Tel: +1 814 865 0036; fax: +1 814 865 8499.
E-mail address: atm2@psu.edu (A.T. Motta).
[1] Currently with the Electric Power Research Institute.
[2] Currently with the Brookhaven National Laboratory.

0022-3115/$ - see front matter © 2009 Elsevier B.V. All rights reserved.
doi:10.1016/j.jnucmat.2009.04.004

metastable γ-hydride was observed in zirconium containing hydrogen concentrations ⩽640 wt ppm [12], while another study examining irradiated Zircaloy-2 cladding found the presence of γ-hydride embedded in predominantly δ-hydride blisters (>10,000 wt ppm) [13,14]. 'Banded, twinned' γ-hydride precipitates were also observed by Barraclough and Beevers in a δ-hydride matrix for stoichiometries of ZrH_x, in the range of $1.3 \leqslant x \leqslant 1.6$, with the volume fraction of γ-hydride approaching zero at $x = 1.6$ (i.e., pure δ-hydride or $ZrH_{1.6}$) [14]. In contrast to these observations, Mishra et al. [15] proposed that the γ-hydride phase is indeed an equilibrium phase resulting from a peritectoid reaction of α-Zr and δ-hydride below ≈255 °C. These data suggest that the γ-hydride and α-Zr are in equilibrium at low temperatures and at hydrogen contents less than 50 atom percent (at.%) or about 10,000 wt ppm. Above this concentration, both γ-hydride and δ-hydride are in equilibrium.

Additionally, at even higher hydrogen concentrations, ε-hydrides (face-centered tetragonal; ZrH_2 with $c_o/a_o < 1$) have been reported [14,16–20,21]. Beck [17] first confirmed the existence of ε-hydride in zirconium by observing a significant decrease in microhardness upon exceeding 62.5 at.% (1.81 wt%) hydrogen, which could only be explained by a phase transformation. This was further evidenced by the apparent divergence of the measured lattice parameters, a_o and c_o, as δ-hydride (fcc) transformed to ε-hydride (fct; where $a_o > c_o$) at 62.5 at.%, or 60.6 at.% according to Barraclough and Beevers [14]. Moreover, Moore and Young [18] found that an equilibrium between δ- and ε-hydride in zirconium occurred between $ZrH_{1.64}$ (≈60 at.%) and $ZrH_{1.74}$ (≈61.5 at.%) at room temperature but the width of this two-phase region decreases with increasing temperature up to 455 °C. Sacedon et al. [22] found both δ- and ε-hydride in massive hydride layers (i.e., pure ZrH_x, where $x > 1.5$; or >15,000 wt ppm) formed in Zircaloy. Nevertheless, all of these studies suggest that a diffusionless martensitic-type transformation explains the δ → ε transformation at even higher contents (ZrH_x, where $x > 1.74$) and upon cooling from higher temperatures [23,19].

More recent studies [24–26] have used X-ray diffraction to investigate the hydride-phase precipitation and stability in Zircaloy-4. Lanzani and Ruch [25] found that only δ-hydride occurred in recrystallized Zircaloy-4 containing 175–1520 wt ppm hydrogen, even after solution and aging treatments. Conversely, Choi et al. [26] showed that both δ- and γ-hydride precipitated for hydrogen contents ranging from 420 to 1140 wt ppm in stress-relieved Zircaloy-4. At even higher hydrogen contents, Veleva et al. [24] also showed mostly δ-hydride at 2000 and 4000 wt ppm but also observed some γ-hydride at 4000 wt ppm. They all however mentioned that the absence of γ-hydride at the lower content may be due to peak intensity associated with this phase being masked by the background intensity or δ-hydride peaks. Based on the results of one study, Lanzani and Ruch [25] concluded that γ-hydride is in fact not an equilibrium phase in Zircaloy-4, suggesting, rather, that it may be a stable phase in higher-purity zirconium, as proposed by Beck [17] and Mishra et al. [15]. Finally, one of these X-ray diffraction studies [24] has observed no appreciable increase in the α-Zr phase diffraction patterns in Zircaloy-4 containing ⩽4000 wt ppm hydrogen, suggesting that hydrides do not introduce a significant strain field or residual stress, contrary to observations of another study [11,27].

These observations suggest that there is not a definitive understanding of the hydride precipitation and actual phase identification in stress-relieved Zircaloy-4 cladding over a range of hydrogen contents, consistent with cladding irradiated to high fuel burnup. In addition, the quantification of hydride content is usually difficult to perform. It is possible to measure the overall hydrogen content of the material and by making assumptions about the hydrogen solubility to infer what the hydride concentration must be. It is also possible to reveal the hydrides by metallographic etching and infer from that measurement a volume fraction. However, true quantification is difficult, as the volume fraction determined from this type of image analysis depends on the etching procedure.

The present study attempts to accurately identify and quantify the hydride phase or phases that precipitate in non-irradiated, stress-relieved Zircaloy-4 cladding so that a better understanding may be developed for such precipitation in high-burnup Zircaloy-4. Cladding samples containing circumferentially-oriented hydrides in two distributions—uniform and localized—across the cladding wall are examined for hydride phase identification using synchrotron X-ray diffraction. Analyses of the diffraction spectra for cladding samples with uniform hydrides are used to quantify the hydride volume fraction, which are correlated to the total hydrogen content of these samples. These examinations and analyses give insight into the hydride precipitation process in Zircaloy-4 cladding and present a technique to quantify the hydride volume fraction using synchrotron radiation.

2. Experimental

2.1. As-received material

Two types of stress-relieved-annealed Zircaloy-4 cladding were obtained from Sandvik Specialty Metals (chemical composition: bal. Zr–1.3Sn–0.23Fe–0.12Cr–0.127O) and Westinghouse (chemical composition: bal. Zr-1.34Sn–0.21Fe–0.11Cr–0.118O) with nominal outer diameter of approximately 9.5 mm and nominal wall thickness of about 0.57 mm (standard 17 × 17-sized-array PWR fuel assembly design). Additionally, AREVA NP also provided stress-relieved Zircaloy-4 cladding tubes (chemical composition: bal. Zr–1.42Sn–0.21Fe–0.10Cr–0.137O) with nominal outer diameter of approximately 10.8 mm and nominal wall thickness of about 0.76 mm (standard 15 × 15-sized-array PWR fuel assembly design). The chemical compositions of Zircaloy-4 cladding materials used in this study were within the specifications given by ASTM Standards for nuclear fuel cladding [28]. No significant differences are expected between the materials furnished by the three suppliers. This was verified by characterizing the material with tensile tests, texture measurements and hardness measurements, to the point that the materials are believed to be essentially similar, so no distinction was kept between the materials during the work. The materials designations are given here for the sake of completeness.

2.2. Hydrogen charging

Zircaloy-4 cladding was hydrogen-charged by gaseous method to produce two distributions of discrete circumferentially-oriented hydride platelets: (i) localized near the outer surface of the cladding in the form of a platelet-dense rim with only a few platelets in the underlying substrate (similar to that of high-fuel-burnup Zircaloy-4) and (ii) uniformly distributed throughout the cladding. Fig. 1 shows examples of these distributions from optical micrographs taken from the radial–transverse (R–T) plane of the hydrided cladding tubes. For both distributions, gas charging was conducted under stress-free conditions to avoid the formation of radially-oriented hydrides (i.e., hydrides platelets with long axis within ±40° of the radial direction of the cladding, as defined by ASTM standard) [28]. The overall hydrogen content (radial average) was measured from approximately 2-mm-wide by 4-mm-long slices (≈0.05-g weight) of cladding rings (approximately 1/4 of circumference) using a inert-gas-fusion process in a LECO Model RH-404 Hydrogen Determinator.

Hydrogen charging to produce 160-mm-long cladding tubes with a hydride rim was conducted by Nuclear Development Corpo-

Please cite this article in press as: R.S. Daum et al., J. Nucl. Mater. (2009), doi:10.1016/j.jnucmat.2009.04.004

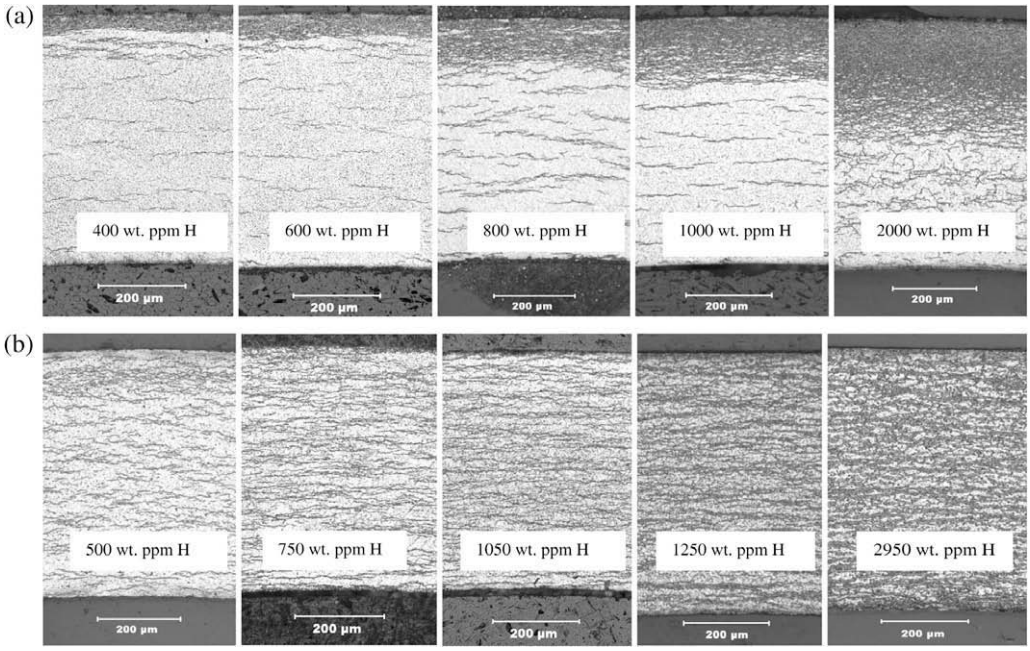

Fig. 1. Radial–transverse optical micrographs showing examples of the two hydride distributions (approximate total hydrogen contents are indicated) in Zircaloy-4 cladding of this study: (a) hydride rim and (b) uniform hydrides. For the hydrides rim samples, the first three are Westinghouse cladding, and the last two Sandvik cladding, while for the uniform hydride samples, the first is Westinghouse, the next two Sandvik and the last two AREVA cladding. The hydrogen contents given are an overall average for the cladding.

ration of Japan as described in [29]. This type of charging resulted in hydride rims with thicknesses ranging from 20 to 300 μm, and total hydrogen contents ranging from 300 to 2200 wt ppm, as illustrated in the optical micrographs in Fig. 1(a).

Hydrogen charging of cladding with a uniform distribution of circumferential hydrides was conducted using a three-zone furnace at 400 °C with flowing 30% hydrogen–70% helium gas mixture at approximately 0.1-MPa positive pressure. Open-ended cladding lengths were pickled in an acid solution, washed with alcohol, and wrapped in aluminum foil, which served as an oxygen getter. The cladding length was then placed within the central heating zone of the furnace and held at 400 °C for various times to facilitate the absorption of the desired amount of hydrogen. The cladding was exposed to the hydrogen–helium gas mixture during heat-up, variable holding times at 400 °C, and then cooled to room temperature at ≈125 °C/h. In some cases, materials were also exposed to pure argon gas during additional heating at 400 °C to ensure homogenization of the hydrogen, and consequently of hydrides. Further details of the hydrogen-charging process are provided elsewhere [30].

2.3. Hydride microstructural characterization

The hydride microstructure was characterized using optical metallography. Samples were mounted and then polished using 240–1200 grit paper followed by 0.5-μm alumina solution. Samples were then etched for 2 min by immersion in an acid solution comprised of 10% hydrofluoric acid, 45% nitric acid, and 45% hydrogen peroxide in order to resolve the hydride microstructure at 100, 200, and 500× under normal lighting conditions.

2.4. Synchrotron X-ray diffraction

Synchrotron X-ray diffraction was employed to identify hydride phases and quantify the contents of these phases in hydrided cladding samples. Diffraction experiments were performed at the 2-BM (bending-magnet) beamline of the Advanced Photon Source (APS) at Argonne National Laboratory. Fig. 2 shows the schematic of the experimental arrangement in this beamline.

Diffraction samples were taken from hydrided Zircaloy-4 cladding tubes cut in half lengthwise and polished (using 800-grit metallographic paper) to reduce the cladding wall to various thicknesses between diffraction runs in order to probe variations in hydrogen content within the hydride rim and underlying substrate of each sample. Samples were oriented such that the X-ray beam was incident on either the longitudinal–transverse (L–T) or the radial–transverse (R–T) sample planes. Fig. 3 schematically shows the orientation of samples, diffracted surfaces (e.g., L–T and R–T planes) with respect to the incident and diffracted X-ray beam. Fig. 3(a) also indicates the wall-thickness reduction of the L–T sam-

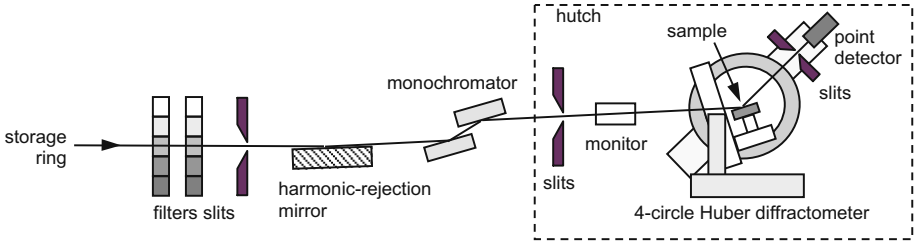

Fig. 2. Schematic of the 2-BM beamline at Advanced Photon Source.

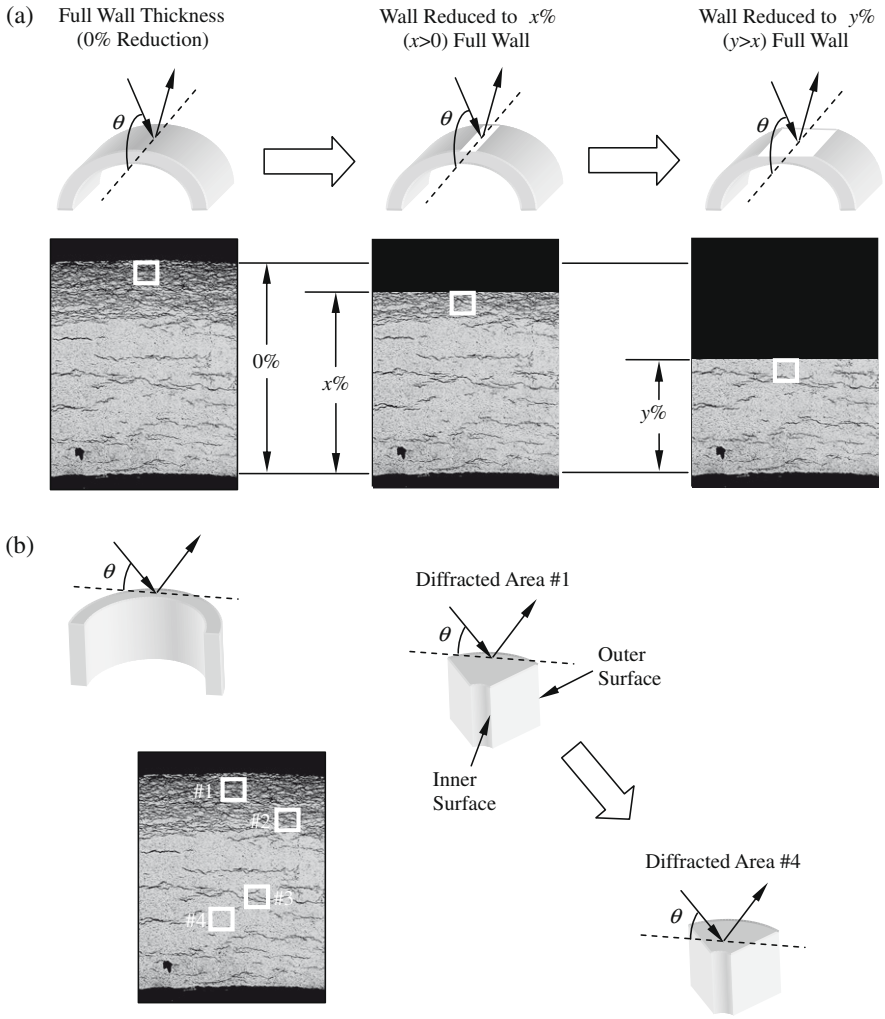

Fig. 3. Schematics showing orientation of diffraction samples with respect to the synchrotron beam (black arrows) incident on (a) longitudinal–transverse (L–T) and (b) radial–transverse (R–T) planes and corresponding hydride microstructure (with and without wall-thickness reduction); note, hydride-rim example and white boxes do not represent the actual size or depth of the beam (Sandvik cladding).

ples in order to obtain the diffracted intensity at locations in the cladding with various hydride densities, as represented by the white boxes. As shown by the white boxes (which are not representative of the scale of the diffracted volume) in Fig. 3(b), diffracted intensity from various hydride densities was also possible for the R–T samples but wall-thickness reduction was not necessary.

Samples were placed on a diffraction stage (i.e., goniometer), with six degrees of movement, including three lineal (x, y, and z) and three rotational (θ, φ, and χ). The diffracted intensity was acquired as a function of 2θ using a scintillation detector mounted on the two-theta arm of the diffractometer. The synchrotron beam used for this study had an energy (E) of 15 keV (0.827-Å wavelength) with an energy band width (dE/E) of approximately 0.01% and a flux of 1.0×10^{10} photons/s. The attenuation length of 15 keV X-rays into Zircaloy is about 65 μm. At an incident angle of 10°, the penetration depth from the surface is approximately 11.3 μm.

Two different X-ray beam sizes were used. A beam size of 2 mm (horizontal) × 1 mm (vertical) was produced by using a pair of slits. A microfocused beam of size 0.015 mm (horizontal) × 0.007 mm (vertical) was obtained by a pair of microfocusing Kirkpatrick-Baez mirrors, placed about 35 cm upstream of the sample. The footprint of the microbeam depends on the incident angle of the beam to the sample surface along the vertical direction. The effective macro- and micro-beam spot sizes for the ranges of 2θ used ($15° \leqslant 2\theta \leqslant 35°$ or $7.5° \leqslant \theta \leqslant 17.5°$) ranged from 3.32 to 7.63 mm and 0.023 to 0.053 mm, respectively. At the beam energy and 2θ angles of this study, the diffracted intensity comes from a volume of cladding to a depth of up to approximately 20 μm below the incident surface. The sample was aligned with respect to the detector and stage motion using both optical and X-ray imaging cameras.

Table 1 lists the crystal properties of the phases of interest in this study. The diffracted intensities for these phases listed in the respective powder diffraction files are shown in Fig. 4, based on the X-ray beam energy of 15 keV used in this study. It is worth noting that many of the peaks associated with γ-, δ-, and ε-hydrides overlap, thus requiring peak deconvolution for proper analysis. Diffraction patterns were obtained at fixed positions within the L–T and R–T planes of the cladding in theta–two theta (θ–2θ) scans. Additional diffraction experiments were conducted along the radial direction of the cladding in the R–T plane at fixed 2θ angles corresponding to selected peaks of the alpha phase and hydrides using the micro-beam condition. Thus the diffracted intensity from a specified peak could be monitored as a function of position relative to the cladding inner and outer surfaces. The linear step size of these radial scans was 1 μm with an acquisition time of 1 s per step.

Please cite this article in press as: R.S. Daum et al., J. Nucl. Mater. (2009), doi:10.1016/j.jnucmat.2009.04.004

Table 1
Properties of various phases present in hydrided Zircaloy-4.

Phase	PDF Nos.	ZrH_x, where $x \approx$	Structure	a_o (nm)	c_o (nm)
α-Zr (matrix)	00-005-0665	0	Hexagonal	0.3232	0.5147
γ-Hydride	00-034-0690	1	Tetragonal	0.4596	0.4969
δ-Hydride	00-034-0649	1.66	Cubic	0.4781	–
ε-Hydride	00-017-0314	2	Tetragonal	0.3520	0.4450

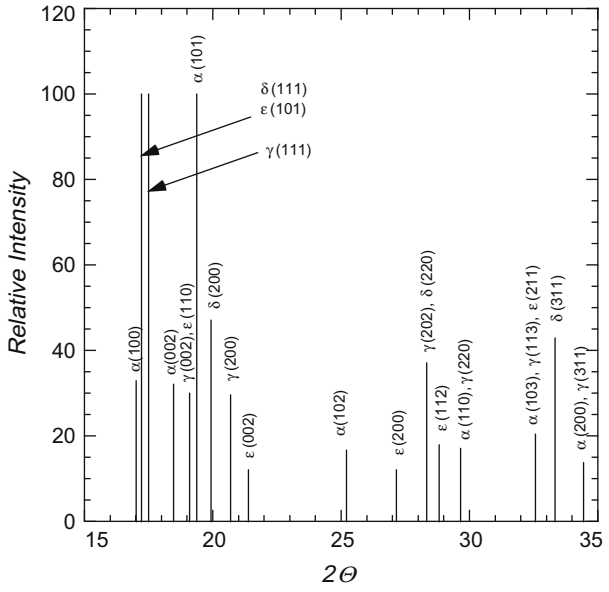

Fig. 4. X-ray diffraction peaks based on data from powder diffraction files for α-Zr, γ-ZrH_x ($x \approx 1$), δ-ZrH_x ($x \approx 1.66$), and ε-ZrH_x ($x \approx 2$) for beam energy of 15 keV; note, for α-Zr, (*hkil*) is reduced to (*hkl*) by assuming $h + k = -i$.

For each specimen, a diffraction pattern was acquired using a low-resolution scan of 2θ angles from 15° to 35° with 400 intervals (or 0.05° per interval) at 1 s per interval. The intention of this low-resolution scan was to confirm the presence of peaks associated with α-Zr phase and hydride phases and localize the subsequent high-resolution scans. This was followed by high-resolution scans of three separate 2θ angular ranges (16.5–21°, 27–29°, and 32–36°) with 0.009° per interval and 1 s counting time per interval. These high-resolution scans were centered on peaks of interest.

The acquired diffraction patterns were analyzed using PeakFit Version 4.12 software to separate the individual diffraction peaks associated with each phase, including overlapping peaks. The centers of the separated peaks were then compared to the expected patterns (Fig. 4) to index peaks and identify phases. Also, the fitting process calculated the area (i.e., integration of diffracted intensity counts after background subtraction) under each separated diffraction peak, using a Pearson VII peak shape. The integrated peak intensities associated with hydrided cladding were normalized to the integrated peak intensities of the α-Zr phase. In doing so, an estimation of the volume fraction for each phase was calculated using the ratios of the integrated intensity according to the following equation [31]:

$$\frac{I_{\delta(111)}}{I_{\alpha(002)}} = \frac{R_{\delta(111)} V_\delta}{R_{\alpha(002)} V_\alpha} \quad \text{and} \quad \frac{I_{\gamma(111)}}{I_{\alpha(002)}} = \frac{R_{\gamma(111)} V_\gamma}{R_{\alpha(002)} V_\alpha}, \tag{1}$$

where $I_{\alpha(hkl)}$, $I_{\delta(hkl)}$, and $I_{\gamma(hkl)}$ are the integrated intensities of the respective *hkl* peaks, and the (V_α, V_δ, and V_γ) are the volume fractions of the α-Zr and the δ- and γ-hydride phases. *R* in Eq. (1) is a factor that relates the volume fraction to the observed diffraction intensities by taking into account the crystallographic properties of each phase and the characteristics of each angle (*hkl*) and is given by:

$$R_{hkl} = \left(\frac{1}{v^2}\right)\left[|F|^2_{hkl} p_{hkl}\left(\frac{1}{\sin^2\theta_{hkl}\cos\theta_{hkl}}\right)\right](e^{-2M})_{hkl}, \tag{2}$$

where, for each peak (*hkl*), *v* is the volume of the unit cell (m^3), $|F|^2_{hkl}$ is the structure factor, p_{hkl} is the multiplicity factor, θ_{hkl} is the Bragg angle for a specific peak, and $(e^{-2M})_{hkl}$ is the temperature factor. For calculating $|F|^2_{hkl}$, the positions of zirconium and hydrogen atoms in the unit cells for α-Zr and γ- and δ-hydrides were taken from literature [31,32]. We note that no account of crystallographic texture in either phase is taken when using this method. A partial justification for this is given in the next section.

3. Results

3.1. Identification of α-Zr diffraction peaks in non-hydrided condition

To properly characterize the evolution of the hydride phases in the cladding materials and as a function of hydrogen content, it is necessary to characterize the diffraction patterns from the α-Zr phase. As discussed previously, two types of stress-relieved Zircaloy-4 cladding were used in this study. Fig. 5 shows indexed diffraction patterns from the L–T planes (see Fig. 3(a)) of the two cladding materials in a non-hydrided condition. These patterns were normalized such that the intensities of the α(0 0 2) diffraction peaks were the same relative intensity (a value set at 100). It is found that the 2θ positions of the α-Zr peaks in the two types of cladding materials differ by no more than 0.027° (Areva) and 0.053° (Sandvik), from the 2θ positions given by the powder diffraction files (PDF) listed in Table 1. The average full width half

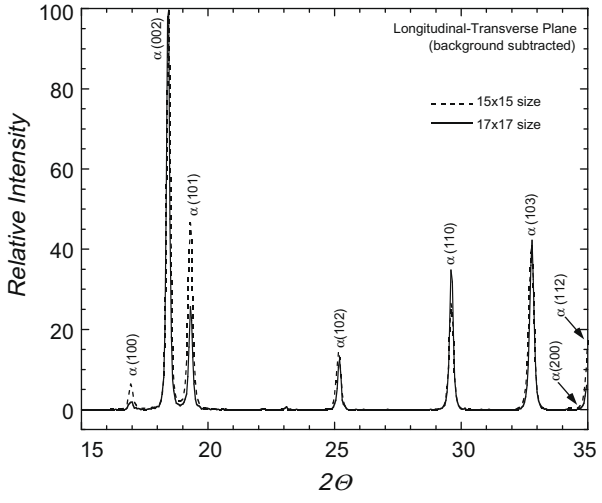

Fig. 5. Diffraction spectra of non-hydrided AREVA and Westinghouse stress-relieved Zircaloy-4 cladding in the longitudinal–transverse (L–T) plane (diffraction vector parallel to the radial direction), showing α-Zr phase peaks in the 2θ range of interest; schematic shows beam incident on L–T plane.

maximum for the α-Zr peaks was 0.198° (Areva) and 0.167° (Sandvik).

Fig. 5 shows diffraction patterns from unhydrided specimens of both type of cladding illustrating the as-fabricated texture (based on relative intensities of the α-Zr peaks). This texture is clearly evident upon comparing the peak intensities in Fig. 5 to those of α-Zr (hexagonal close-packed alpha phase) powder diffraction pattern of Fig. 4. In particular, the α(1 0 1) is three times more intense than both the α(1 0 0) and α(0 0 2) peaks in the random sample. In the textured tube, the highest intensity in the L–T measurement is that of the α(0 0 2) basal pole, reflecting the fact that more poles tend to align with the radial or normal direction of the cladding during processing. The α(1 0 0) intensity is very low as a consequence, and the α(1 0 1) intensity is significantly diminished relative to the random value. Thus it appears that both materials exhibit similar textures, with the normals to the basal planes having the highest diffracted intensity in the L–T plane (or radial normal).

3.2. Hydride phase identification in cladding with uniform hydrides

Fig. 6 shows diffraction patterns obtained in the L–T plane for the uniformly-hydrided cladding containing varying hydrogen contents. The diffraction patterns for each hydrogen content were again normalized to the highest intensity; in this case, the α(0 0 2) peak. Cladding samples with hydrogen contents of ≈10 (non-hydrided control), 250, 670, 1250, and 2950 wt ppm were scanned to determine the effect of hydrogen content on the change in the integrated intensities, 2θ positions, and full-width at half maximum (FWHM) of the α-Zr and hydride peaks. The 2θ positions of these peaks are also compared to those in the appropriate powder diffraction files.

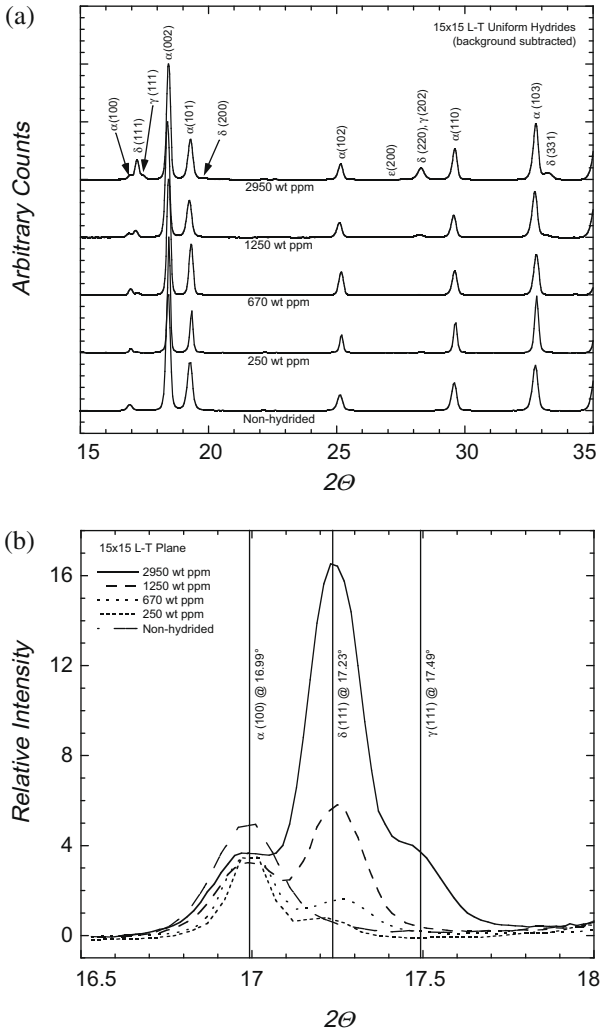

Fig. 6. (a) Low- and (b) high-resolution diffraction patterns of AREVA cladding with uniform distribution of hydrides and containing various hydrogen contents, showing peaks associated with α-Zr and γ- and δ-hydride phases; solid vertical lines in (b) show 2θ positions of the labeled phases with (*hkl*)-designated planes based on data from powder diffraction files.

In addition to the peaks associated with α-Zr, the other peaks observed were consistent with δ- and γ-hydride phases listed in the literature. The γ-hydride phase was only seen at higher hydrogen contents, and the ε-hydride phase was not observed. As hydrogen content increases, the intensities of the peaks associated with the δ-hydride phase increase, and at contents >1250 wt ppm, peaks associated with the γ-hydride phase are also seen. This effect is more easily seen in Fig. 6(b), which clearly shows the increasing integrated intensity of the δ(1 1 1) peak, (at a 2θ position of 17.23°), with increasing hydrogen content. Although a peak associated with ε-hydride exists at the same location, the peak located at 17.23° is assumed to be entirely associated with the δ(1 1 1) plane. This assignment is based on the fact that the ε(2 0 0) peak, (located at a 2θ position of ≈27.17°) is not observed up to 3000-wt-ppm hydrogen.

Fig. 7 shows examples of these fits and their residuals (i.e., difference between the fitted curve and the measured intensities) for the samples shown in Fig. 6. The 2θ positions of the α-Zr peaks are consistent with those listed in the PDF even with increasing hydrogen content, with possibly a slight (≈0.03°) shift in the lower 2θ direction for the pyramidal planes (e.g., α(1 0 1), α(1 0 2), and α(1 0 3)). The positions of the basal plane and prismatic (e.g., α(1 0 0), α(110)) are not affected. As the hydrogen content increases, the FWHM of the α-Zr peaks also increase, with a marked increase between the non-hydrided sample (≈10-wt-ppm hydrogen) and the 670-wt-ppm sample. Because it is possible that hydride platelets grow with increasing hydrogen content, it is also possible that the peak broadening (i.e., increase in FWHM) is caused by non-uniform residual matrix strain brought about by the precipitation of hydrides. It is important to note that there is an increase in volume of 17.2% for δ-hydride and 12.3% for γ-hydride compared to the α-Zr matrix [11]. The combination of the slight shift in 2θ position and peak broadening of α(*hkl*) pyramidal planes suggests that the precipitation of macroscopically-large hydrides (i.e., hydrides with platelet dimensions greater than the dimensions of the α-Zr grains) induces strains in the matrix, as suggested previously [27].

The diffraction patterns in Figs. 6 and 7 indicate that δ-hydride is the predominant hydride phase for hydrogen contents ⩽3000 wt ppm. Furthermore, peaks associated with the γ-hydride phase are only observed at contents >1250-wt-ppm hydrogen. Lastly, no evidence of ε-hydride phase was found for hydrogen contents <3000 wt ppm.

3.3. Hydride phase identification in cladding with hydride rims

Hydrides were also studied in samples with non-uniform hydride distribution, such as a hydride rim (see Fig. 1). Using the technique illustrated in Fig. 3(a), phases in the hydride rim and underlying substrate were determined in separate diffraction scans. In some cases, diffraction patterns were obtained from depths in the hydride rim with different hydride densities (or volume fraction), and thus, hydrogen contents. The effect of hydride precipitation on the 2θ positions and FWHM of the hydride phases and α-Zr peaks was also investigated by comparing to non-hydrided controls, as was done for uniformly-hydrided samples in the previous section.

Please cite this article in press as: R.S. Daum et al., J. Nucl. Mater. (2009), doi:10.1016/j.jnucmat.2009.04.004

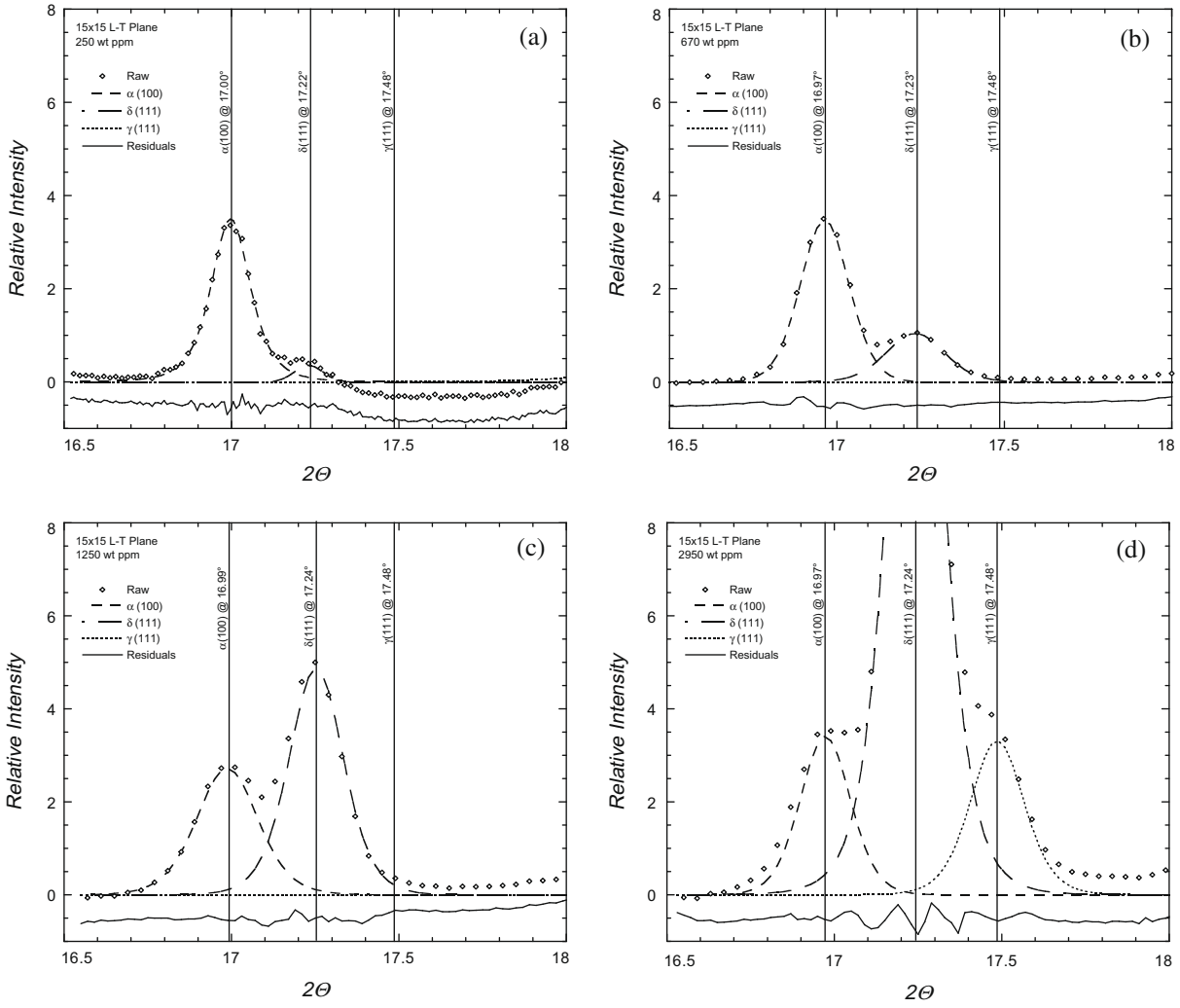

Fig. 7. Peak fitting analysis of individual peaks from high-resolution patterns for (a) 250, (b) 670, (c) 1250, and (d) 2950-wt-ppm-hydrogen cases given in Fig. 6.

Fig. 8 shows diffraction patterns (normalized to α(0 0 2) peak intensity) taken in the L–T orientation (see Fig. 3(a)) for cladding containing hydride rims with thicknesses of ≈40 μm in Fig. 8(a) (corresponding to 400-wt-ppm image in Fig. 1(a)) and ≈260 μm in Fig. 8(b) (corresponding to 2000-wt-ppm image in Fig. 1(a)). The samples were successively polished so that different depths could be probed, from the top of the hydride rim to the substrate. Cladding with intermediate hydride-rim thicknesses showed comparable results.

Because the penetration of the X-ray beam (less than ~12 μm, as discussed above) is smaller than the hydride rim thickness, the top pattern in either case is representative of the hydride concentrations in the rim. Fig. 8 shows that peaks associated with the δ-hydride phase including δ(1 1 1), δ(2 0 0) and δ(3 3 1) are seen in all regions (hydride rim, high hydrogen and low hydrogen regions and substrate). The peaks are very strong in the hydride rims, and comparatively lower in the low hydride part of the rim (see figure). The substrate shows some hydride peaks, but their intensity is much lower. In contrast, the ε-hydride phase is only observed in the 260-μm-thick rim: the ε(2 0 0) peak (located at 2θ position of ≈27.17°) is absent in the 40-μm-thick rim (see Fig. 8(a)) and present in the 260-μm-thick rim (see Fig. 8(b)). The peak labeled as δ(2 0 0) in Fig. 8(a) at a 2θ position of ≈20° shows significant broadening and asymmetry, both of which could be due to the presence of both the δ(2 0 0) (located at ≈19.90°) and γ(2 0 0) (located at ≈20.72°), but the γ(2 0 0) peak was not observed in any of the other diffraction patterns.

As in the uniformly-hydrided cladding containing ≈2950-wt-ppm hydrogen (see Fig. 7(d)), the γ-hydride phase is seen in the hydride-rim cladding by the increasing intensity of a shoulder to the right of the δ(1 1 1) peak at a 2θ position of ≈17.5°, which corresponds to the expected 2θ position of the γ(1 1 1) peak (see Fig. 8). Fig. 9 shows the increasing intensity of the γ(1 1 1) peak with increasing hydrogen content. The positions of the δ-hydride peaks appear to shift by 0.02–0.04° toward higher 2θ between the low hydrogen-content rim and the high hydrogen-content rim. It is possible that this shift is caused by compressive stresses from hydride formation. Conversely, the 2θ positions of the α-Zr peaks are unchanged with hydrogen content.

It is possible to more clearly identify the γ(1 1 1) peak by fitting the raw diffraction patterns to deconvolute the peaks. The deconvolution can also help identify the ε-phase. Because the δ(1 1 1) and ε(1 0 1) peaks completely overlap each other, the distinction between δ- and ε-hydride is made based on the ε(2 0 0) peak. Fig. 10 shows examples of the diffraction patterns (data points) from Fig. 9 and the fits with the corresponding residuals (at the bottom of each fit). The vertical lines in Fig. 10 indicate the 2θ-position center of the fitted peaks which compare well with literature values. Similarly to what occurs with the δ(1 1 1) peak, the height and area (i.e., integrated intensity) of the fitted γ(1 1 1) peak increases with the hydride density or local hydrogen content. The

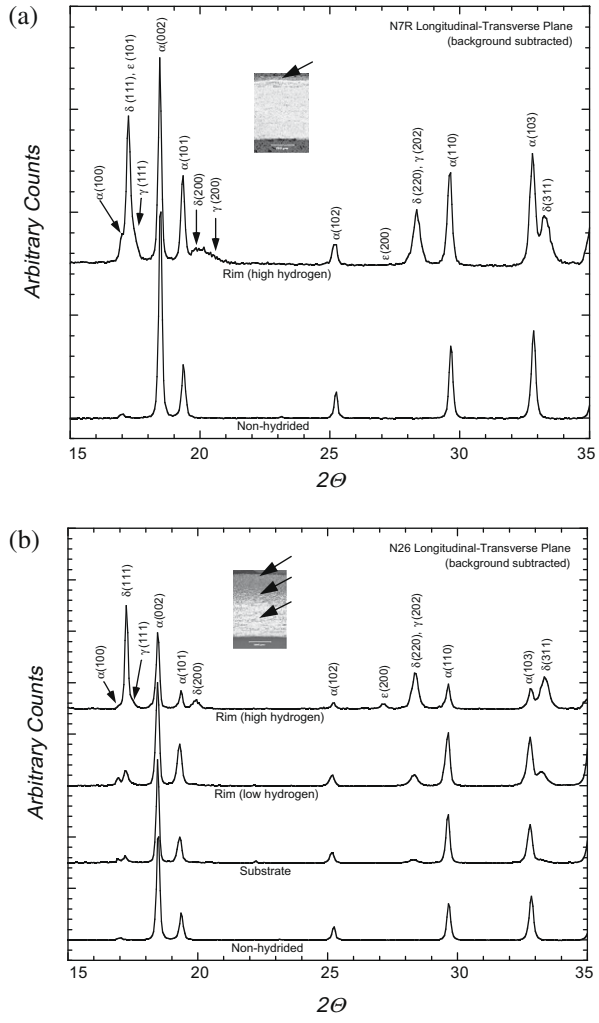

Fig. 8. Diffraction patterns from the L–T plane of cladding with hydride-rim thicknesses (radial-average hydrogen content) of (a) ≈40 μm (≈400 wt ppm) (Westinghouse cladding) and (b) ≈260 μm (≈2000 wt ppm) (Sandvik cladding); arrows in inset micrographs show depths after polishing from where patterns were taken. Non-hydrided patterns are also shown for comparison.

highest hydrogen content in the hydride rim (see Fig. 10(a)) shows a significant γ(1 1 1) peak, whereas, this same peak is negligible for the relatively hydride-free substrate (see Fig. 10(c)). As expected, the non-hydrided cladding does not show a peak associated with either δ(1 1 1) or γ(1 1 1) (see Fig. 10(d)). The effect of hydrogen content on peak intensity and, more importantly, integrated peak area will be addressed in following section.

Comparing the intensities of individual peaks in the diffraction patterns of hydrided cladding obtained in cross-section (i.e., R–T orientation) is another method for determining the extent of hydride precipitation and phase in hydride-rim cladding. This method involved the translation of the micro-beam along the radial direction of cladding in the R–T plane to determine the variation of specific peaks with depth (see Fig. 3(b)). This radial translation was conducted at fixed 2θ values corresponding to α(1 0 1), δ(1 1 1), and γ(1 1 1) peaks. Unfortunately, because the presence of ε-hydride was not suspected at the start of the experiment, scans of the ε(2 0 0) peak were not acquired. The purpose of this method was to understand the precipitation of phases within the substrate and the hydride rim for comparison with the metallographic examination; (Fig. 1). Fig. 11(a)–(c) shows such scans for specimens containing hydride rims with thicknesses of ≈60, 150, and 220 μm (≈850, 1000, and 2000-

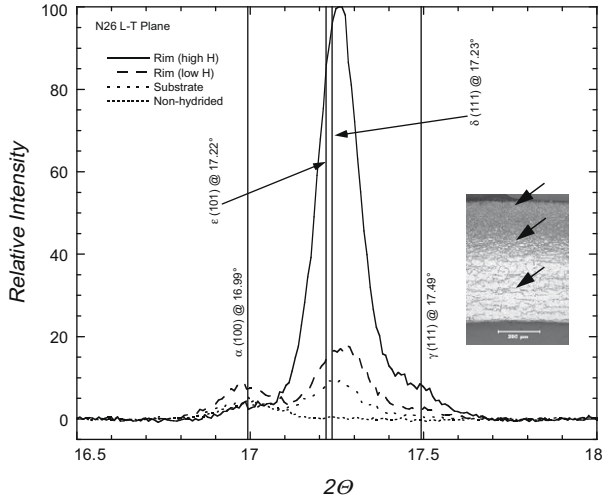

Fig. 9. High-resolution diffraction patterns of hydride-rim Sandvik cladding containing a ≈260-μm-thick hydride rim (≈2000-wt-ppm radial-averaged hydrogen content) showing peaks associated with α(1 0 0), ε(1 0 1), δ(1 1 1) and γ(1 1 1) planes; solid vertical lines show 2θ positions of these planes based on data from PDF; arrows in inset micrographs show depths after polishing from where patterns were taken. Non-hydrided patterns are also shown for comparison.

wt-ppm total hydrogen content, respectively). Fig. 11(d) shows a scan obtained from a specimen with uniform hydrides and containing ≈1250-wt-ppm hydrogen (see Fig. 1(b)) for comparison to the hydride-rim material.

The hydride rim is clearly discernible by the increase in intensity of the δ(1 1 1) and γ(1 1 1) peaks near the surface in Figs. 11(a)–(c). Moreover, in the substrate and the uniformly-distributed specimen, the diffraction signal is uniform, but local variations in hydride concentrations are made evident by the presence of the local fluctuations in the intensity of the δ(1 1 1) and γ(1 1 1) signal. The γ(1 1 1) signals in Fig. 11 are somewhat misleading since this phase is not directly observed in the substrates, and in most cases, the regions of the hydride rims with contents <1250-wt-ppm hydrogen (as indicated by the results from uniformly-hydrided specimens). In fact, most of the intensity corresponding to the γ(1 1 1) peak is likely due to the intensity associated with the shoulder of the δ(1 1 1) peak (note, this is a log scale plot). However, peak fitting analysis does show a discernible γ(1 1 1) peak in the higher hydrogen contents of the hydride rim (see Fig. 10). The analysis suggests that, depending on hydride density, the γ-hydride phase is present in region of the rim nearest to the outer surface. This is best seen in Fig. 11(c) by observing the marked increase in the γ(1 1 1) signal at ≈35 μm from the outer surface. This increase may be quantified by taking the ratio of raw intensities of the γ(1 1 1) to the δ(1 1 1) (i.e., $i_{\gamma(111)}/i_{\delta(111)}$) in the two regions of the rim. Within 35 μm of the outer surface, the $i_{\gamma(111)}/i_{\delta(111)}$ ratio is ~0.19 but drops to ~0.11 in the remainder of the hydride rim to a depth of 220 μm. Lastly, the ε-hydride phase was not scanned for in the hydride rims of specimens corresponding to Figs. 11(a), (b), and (d), but was observed using L–T scans (see Fig. 8(b)) in the region of the rim near the outer surface for the specimen corresponding to Fig. 11(c).

A final check was performed by measuring the overall hydrogen content of hydrides rim samples with intact rim, partially removed rim and completely removed rim (see Fig. 3(a)). By equating the hydrogen content measured on this last one with the hydrogen content in the substrate value, it is possible to evaluate the hydride content of the rim using the measured rim thickness from metallography. This was done for the sample in Fig. 3(a) and the hydrogen content in the rim was calculated to be 2700 wt ppm for both the unremoved and partially removed rim. This value and the sub-

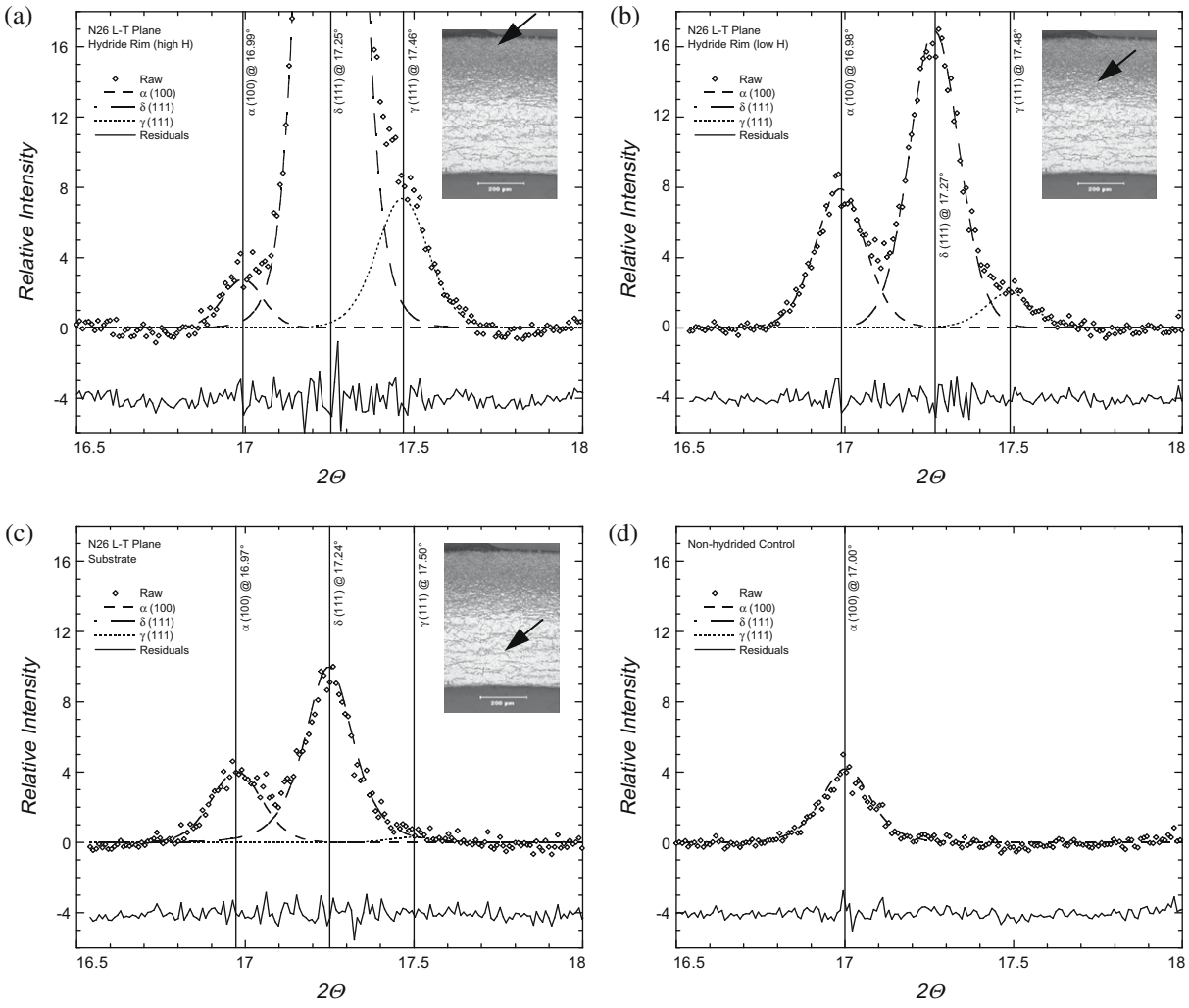

Fig. 10. Diffracted intensity data and fits of individual peaks from spectra of Sandvik cladding with hydride-rim thickness of ≈260 μm (≈2000 wt ppm hydrogen) (a) hydride rim (high H), (b) hydride rim (low H), (c) substrate, and (d) non-hydrided control given in Fig. 9; arrows in inset micrographs show depths after polishing from where diffraction patterns were taken.

strate value are in good agreement with measurements performed in the uniformly-hydrided samples [30].

4. Analysis and discussion

The results of this and the previous section suggest an evolution of hydride-phase content with increasing hydrogen content. In particular, cladding with uniform distribution of hydrides at hydrogen contents up to ≈3000 wt ppm show γ- and δ-hydride peaks but the ε(2 0 0) peak was not observed. It appears that the γ-hydride phase begins to precipitate at hydrogen contents >1250 wt ppm. However, since intermediate contents were not analyzed, this threshold is not well defined. The ε(2 0 0) peak, which is the only unequivocal indication of the ε-hydride phase available, only appears in hydride rims with high hydride density.

The presence of metastable γ-hydride in the uniformly hydrided material is not that surprising given that the cooling rate (>2 °C/min) of the hydrogen-charging treatment is comparable to that mentioned in literature [10,17]. More interesting is the increasing intensity associated with the γ(1 1 1) peak with increasing hydrogen content above some threshold content. This latter point is in good agreement with previous observations [13,14].

To quantify the hydride-phase content from the diffraction patterns, a correlation was made between the integrated intensities of the α(0 0 2), δ(1 1 1), and γ(1 1 1) peaks from uniformly-hydrided samples to the volume fractions of each phase; ε-hydride phase was not observed in these uniformly-hydrided samples but this analysis includes calculations for this phase. The total hydrogen contents of these samples measured by inert gas fusion were related to the volume fraction by assuming only δ-hydride precipitation with <1250-wt-ppm hydrogen. This type of correlation is referred to as the *direct comparison method* [33] and uses the formulation shown in Eq. (1). Table 2 lists the parameters for α-Zr phase and the γ-, δ-, and ε-hydride phases used to calculate *R*-values (the value of $R_{\varepsilon(200)}$ was also calculated for completeness).

Fig. 12 shows the measured volume fraction ratios (V_δ/V_α) and (V_γ/V_α) as a function of the total hydrogen content for the uniformly-hydrided claddings, using Eq. (1). The calculated values (filed symbols), included for comparison, are from the measured total hydrogen contents ($[H]_{total}$) converted to hydride volume fraction V_{ZrH_x} assuming only δ-hydride precipitation using the following [34]:

$$[H]_{total} = [H]_\delta \cdot V_\delta \cdot \left[\frac{\rho_\delta}{\rho_{\alpha-Zr}\cdot(1-V_\delta)+\rho_\delta \cdot V_\delta}\right], \quad (3)$$

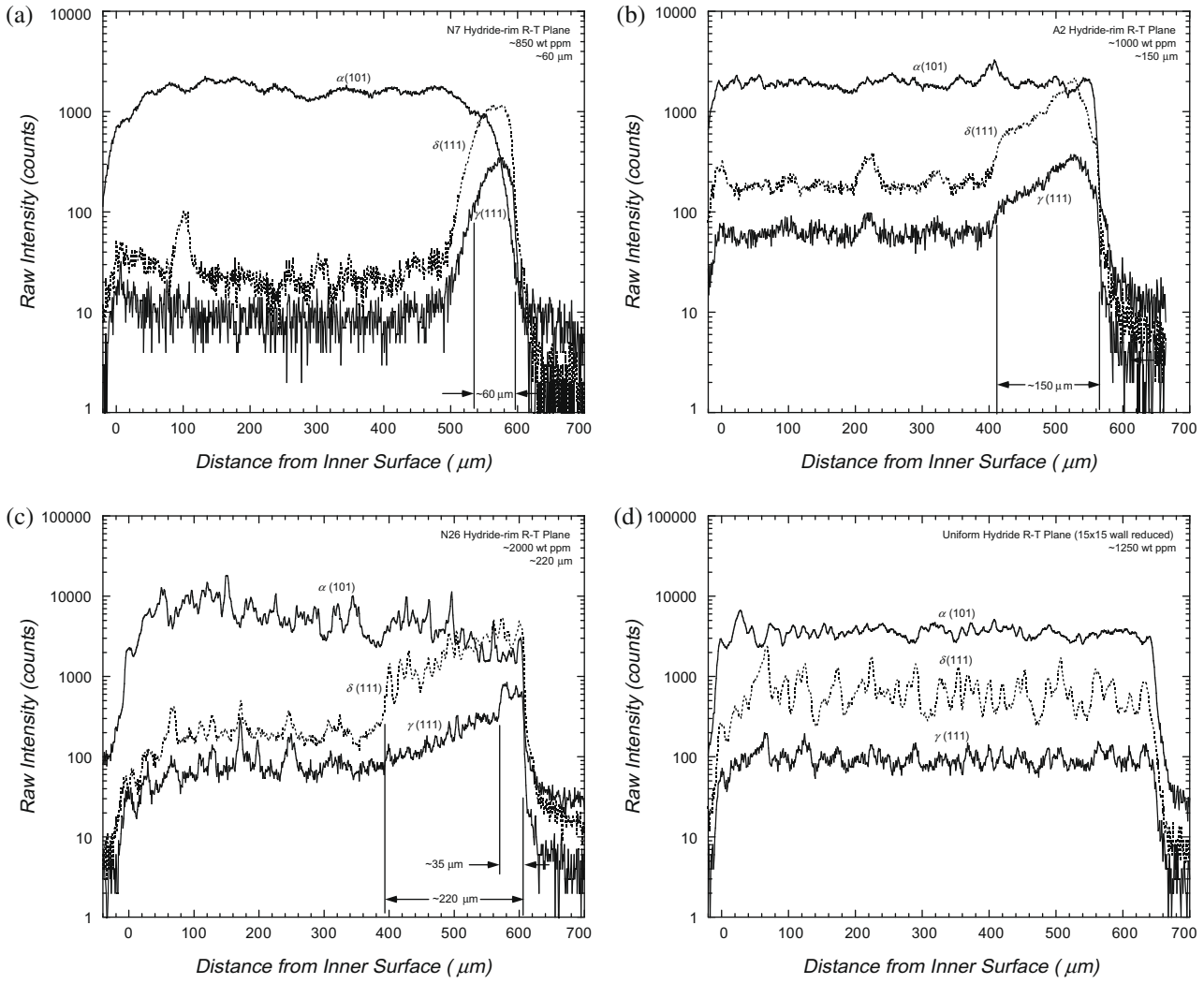

Fig. 11. Radial line scans of α(1 0 1), δ(1 1 1), and γ(1 1 1) peak intensity across cladding wall for specimens with hydride-rim thicknesses of (a) ≈60, (b) ≈150, (c) ≈220 wt ppm hydrogen and (d) a specimen with uniform hydrides (1250-wt-ppm hydrogen); note, (d) is AREVA-size cladding, whereas, (a) is Westinghouse, and (b) and (c) are Sandvik cladding.

Table 2
Parameters for α-Zr and hydride phases for selected (*hkl*) planes at room temperature used in the calculations of *R*-values for Eq. (1).

Parameter (units)	Phase(*hkl*)			
	α(0 0 2)	γ(1 1 1)	δ(1 1 1)	ε(2 0 0)
Crystal structure	HCP	FCT	FCC	FCT
Volume of unit cell, v (m^3)	4.656×10^{-29}	1.041×10^{-28}	1.093×10^{-28}	5.514×10^{-29}
Density, ρ (g/cm^3)	6.51[a]	5.837[b]	5.646[b]	5.617[b]
Atomic/molecular weight (amu)	91.220[a]	92.228[b]	92.893[b]	93.236[b]
Form factor, $f_{Zr}(hkl)$ (unitless)[c]	31.12	31.69	31.84	26.77
Form factor, $f_H(hkl)$ (unitless)[c]	–	0.534 (1 1 1)	0.542 (1 1 1)	0.287 (2 0 0)
Structure factor, $\|F(hkl)\|^2$ (unitless)[d]	1.55×10^4	1.66×10^4	1.73×10^4	1.17×10^4
Multiplicity factor, $p(hkl)$ (unitless)	2	8	8	4
Mean square atomic displacement, u^2 (nm^2)[e]	0.0001 for Zr	0.0002 for H		
Temperature factor, $e^{-2M}(hkl)$ (unitless)	0.942	0.899	0.902	0.775
Calculated *R* factor (nm^{-6})[f]	0.001057	0.000967	0.000944	0.000445

[a] From [33]; also listed, the density of atomic hydrogen, $\rho_H \approx 0.08375 \times 10^{-3}$ g/cm^3.
[b] From [35].
[c] Linear interpolation from data given in [33].
[d] Based on atomic positions of α-Zr [33] and ZrD_x [32].
[e] From powder neutron diffraction of Zr-Co-D alloy in [36].
[f] Calculated using Eq. (2).

where $[H]_{\delta l}$ is the hydrogen content of the δ-hydride phase, ρ_δ is the density of δ-hydride phase at room temperature, and $\rho_{\alpha\text{-Zr}}$ is the density of α-Zr phase at room temperature. The measured and calculated values of (V_δ/V_α) agree quite well in the lower hydrogen

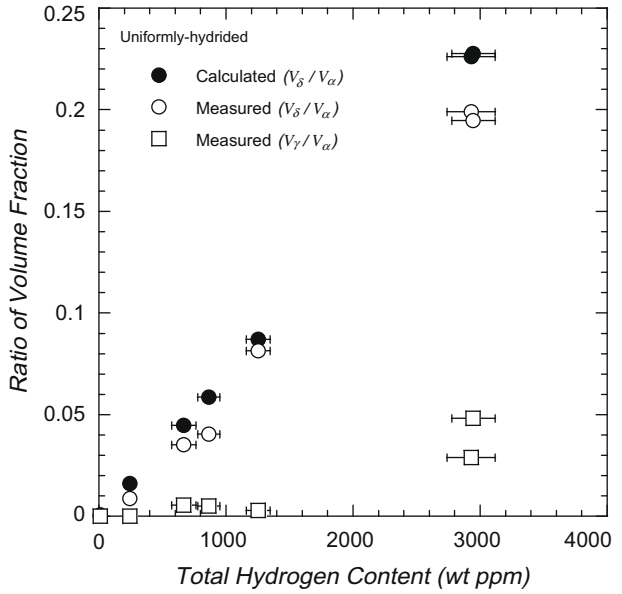

Fig. 12. Ratio of volume fractions (V_δ/V_α) and (V_γ/V_α) measured from the integrated diffracted intensities (Eq. (1)) and same ratio calculated from the total hydrogen content converted to all δ-hydride (Eq. (3)).

content range and differ by ≈10% at the higher hydrogen contents. This difference is likely due to the fact γ-hydride precipitation occurs at higher hydrogen contents, as shown in Fig. 12. These results suggest that synchrotron radiation diffraction (with or without a microbeam) can be used to quantify hydride volume fraction in zirconium alloy cladding.

5. Conclusions

Hydrided stress-relieved Zircaloy-4 cladding tubes were analyzed using synchrotron X-ray diffraction in order to identify the hydride phases present for two distributions of hydrides: (i) circumferential hydride platelets concentrated in the form of a localized hydride rim at the outer surface of the cladding (to simulate the hydride distribution found in high-burnup Zircaloy-4 cladding) and (ii) circumferential hydrides uniformly distributed across the cladding wall. Cladding tube samples of various hydride-rim thicknesses (20–260 μm) and total hydrogen contents (300–2200 wt ppm) were examined. The volume fraction of hydride phases were quantified through a correlation of diffracted integrated intensities and measured hydrogen contents from inert gas fusion. The following are the general conclusions of this study:

- The locations of diffraction peaks observed (associated with the α-Zr matrix and the δ-, γ-, and ε-hydride phases) agreed well with those given in the Powder Diffraction File.
- The δ-hydride phase was observed predominantly in the Zircaloy-4 cladding of this study, but in hydride rims and uniformly-hydrided cladding with hydrogen contents between 1250 and 3000-wt-ppm hydrogen, both γ- and δ-hydrides were seen.
- All three hydride phases (δ, γ and ε) were detected in hydride rims containing >3000-wt-ppm hydrogen, but the exact threshold content for ε-hydride formation was not determined.
- The hydride volume fraction was estimated using the integrated intensities of selected δ- and γ-hydride diffraction peaks normalized to a selected α-Zr peak and was shown to have excellent agreement with volume fractions calculated from measured total hydrogen content up to 1250 wt ppm.

Acknowledgements

The authors would like to acknowledge Yong Yan and Yuncheng Zhong of Argonne National Laboratory for their assistance with the experimental work of this study. The authors also acknowledge helpful discussions with D. Koss. The authors also thank NDC, Areva and Sandvik for supplying the hydrided Zircaloy and Zircaloy samples used in this study. This research was supported by US Nuclear Regulatory Commission, Office of Nuclear Regulatory Research. Usage of the Advanced Photon Source was supported by the US Department of Energy, Office of Basic Energy Sciences under Contract No. DE-AC02-06CH11357.

References

[1] C. Lemaignan, A.T. Motta, Zirconium alloys in nuclear applications, in: B.R.T. Frost (Ed.), Materials Science and Technology, A Comprehensive Treatment, vol. 10B, VCH, New York, 1994, p. 1.
[2] J.R. Secker, B.J. Johansen, D.L. Stucker, O. Ozer, K. Ivanov, S. Yilmaz, E.H. Young, Nucl. Technol. 151 (2005) 109.
[3] R.O. Meyer, R.K. McCardell, H.M. Chung, D.J. Diamond, H.H. Scott, Nucl. Saf. 37 (1996) 372.
[4] L.F.Van Swam, A.A. Strasser, J.D. Cook, J.M. Burger, Behavior of Zircaloy-4 and zirconium liner Zircaloy-4 cladding at high burnup, in: 1997 LWR Fuel Performance Meeting, Portland, OR, 1997, p. 421.
[5] A.M. Garde, G.P. Smith, R.C. Pirek, In-PWR irradiation performance of dilute tin–zirconium advanced alloys, in: Zirconium in the Nuclear Industry: Thirteenth International Symposium (ASTM STP 1423), 2002, p. 490.
[6] A. McMinn, E.C. Darby, J.S. Schofield, The terminal solid solubility of hydrogen in zirconium alloys, in: Zirconium in the Nuclear Industry: Twelfth International Symposium, ASTM STP 1354, 2000, p. 173.
[7] J.J. Kearns, J. Nucl. Mater. 22 (1967) 292.
[8] C.E. Ells, J. Nucl. Mater. 28 (1968) 129.
[9] B. Nath, G.W. Lorimer, N. Ridley, J. Nucl. Mater. 49 (1973) 262.
[10] J.S. Bradbrook, G.W. Lorimer, N. Ridley, J. Nucl. Mater. 42 (1972) 142.
[11] G.J.C. Carpenter, J. Nucl. Mater. 48 (1973) 264.
[12] B. Nath, G.W. Lorimer, N. Ridley, J. Nucl. Mater. 58 (1975) 153.
[13] M.R. Warren, D.K. Bhattacharya, J. Nucl. Mater. 56 (1975) 121.
[14] K.G. Barraclough, C.J. Beevers, J. Nucl. Mater. 34 (1970) 125.
[15] S. Mishra, K.S. Sivaramakrishnan, M.K. Asundi, J. Nucl. Mater. 45 (1972) 235.
[16] W.A. Backofen, Deformation Processing, Addison-Wesley Publishing Co., Reading, MA, 1972.
[17] R.L. Beck, Trans. ASM 55 (1962) 542.
[18] K.E. Moore, W.A. Young, J. Nucl. Mater. 27 (1968) 316.
[19] M.P. Cassidy, C.M. Wayman, Metall. Trans. A 11A (1980) 47.
[20] C.P. Kempter, R.O. Elliot, K.A. Geschneidner, J. Chem. Phys. 33 (1960) 837.
[21] C. Domain, R. Besson, A. Legris, Acta Metall. 52 (2004) 1495.
[22] J.L. Sacedon, M. Diaz, J.S. Moya, B. Remartinez, J. Izquierdo, J. Nucl. Mater. 327 (2004) 11.
[23] D.O. Northwood, U. Kosasih, Int. Metals Rev. 28 (1983) 92.
[24] M. Veleva, S. Arsene, M.C. Record, J.L. Bechade, J. Bai, Metall. Mater. Trans. A 34A (2003) 567.
[25] L. Lanzani, M. Ruch, J. Nucl. Mater. 324 (2004) 165.
[26] Y. Choi, J.W. Lee, Y.W. Lee, S.I. Hong, J. Nucl. Mater. 256 (1998) 124.
[27] G.J.C. Carpenter, J.F. Watters, R.W. Gilbert, J. Nucl. Mater. 48 (1973) 267.
[28] ASTM, B811-97, Standard specification for wrought zirconium alloy seamless tubes for nuclear reactor fuel cladding, West Conshohocken, PA, 1997.
[29] F. Nagase, H. Uetsuka, Hydride morphology and hydrogen embrittlement of Zircaloy fuel cladding used in NSRR/HBO experiment, in: Proceedings of the ANS International Topical Meeting on Light Water Reactor Performance, Portland, OR, ANS, 1997, p. 677.
[30] R.S. Daum, Hydride Induced Embrittlement of Zircaloy-4 Under Plane Strain Tension Testing, PhD Thesis in Materials Science, Penn State University, 2007.
[31] B.D. Cullity, Elements of X-ray Diffraction, Addison-Wesley, Reading, MA, 1978.
[32] S.S. Sidhu, N.S. Satya Murthy, F.P. Campos, D.D. Zauberis, Neutron and X-ray diffraction studies of nonstoichiometric metal hydrides, in: 141st Meeting of the American Chemical Society, Washington, DC, 21–23 March, 1962, p. 87.
[33] B.D. Cullity, Elements of X-ray Diffraction, 2nd Ed., Addison-Wesley Publishing Company, Inc., 1978.
[34] D.I. Schrire, J.H. Pearce, Scanning electron microscope techniques for studying Zircaloy corrosion and hydriding, in: Zirconium in the Nuclear Industry: Tenth International Symposium, ASTM STP 1245, 1994, p. 98.
[35] I.F. Ferguson, Computed x-ray powder diffraction patterns and densities for corundum, aluminium, zirconium, delta-UZr2, and the zirconium hydrides, TRG Report 2438(s), United Kingdom Atomic Energy Authority, 1976.
[36] A.B. Riabov, V.A. Yartys, H. Fjellvag, B.C. Hauback, M.H. Sorby, J. Alloys Compd. 296 (2000) 312.